ACS APPLIED MATERIALS & INTERFACES

www.acsami.org

Research Article

Replicable Quasi-Three-Dimensional Plasmonic Nanoantennas for Infrared Bandpass Filtering

Bongjoong Kim,[#] Jehwan Hwang,[#] Jonghun Yi, Dong Rip Kim, Augustine Urbas, Zahyun Ku,* and Chi Hwan Lee*

Cite This: *ACS Appl. Mater. Interfaces* 2021, 13, 24024−24031

Read Online

ACCESS | Metrics & More | Article Recommendations | Supporting Information

ABSTRACT: Quasi-three-dimensionally designed metal−dielectric hybrid nanoantennas have provided a unique capability to control light at the nanoscale beyond the diffraction limit, which has enabled powerful optical manipulation techniques. However, the fabrication of these nanoantennas has largely relied on the use of nanolithography techniques that are time- and cost-consuming, impeding their application in wide-ranging use. Herein, we report a versatile methodology enabling the repetitive replication of these nanoantennas from their silicon molds with tailored optical features for infrared bandpass filtering. Comprehensive experimental and computational analyses revealed the underlying mechanism of this methodology and also provided a technical guideline for pragmatic translation into infrared filters in multispectral imaging.

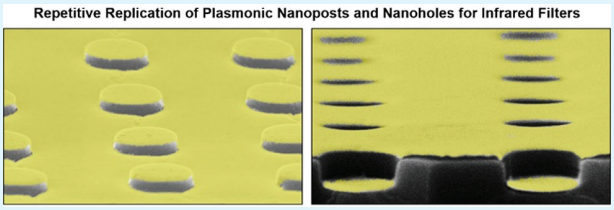

KEYWORDS: *replicable nanoarchitectures, quasi-3D plasmonic nanoantennas, infrared bandpass filter, nanofabrication, nanoantenna, metamaterials*

INTRODUCTION

Bandpass filters that allow through a specific band of light wavelengths serve as a critical optical element of spectral imaging for broad applications including space-based imaging, remote sensing, military target tracking, land mine detection, diagnostic medicine, and environmental monitoring.[1−5] The bandpass filters are typically composed of coupled half-wavelength resonators and multilayer mirrors using alternating dielectric thin films with high and low refractive indices to form a Fabry−Perot optical cavity.[6,7] Effective bandpass filtering occurs through the constructive interference of light when a phase difference coincides with incoming and reflected light waves.[8] Narrow bandpass filtering with tunable spectral selectivity occurs using hybrid metal−dielectric plasmonic nanoarchitectures (i.e., nanoantennas) with various structural configurations such as metal disks, metal holes, metal coaxial apertures, split-ring resonators, coherent perfect absorbers, and quasi-three-dimensional (quasi-3D) crystals.[9−16] These plasmonic nanoantennas enable a surface-plasmon-enhanced light transmission through a subwavelength aperture (i.e., extraordinary optical transmission).[17]

Traditionally, the fabrication of these plasmonic nanoantennas has primarily relied on the use of conventional nanolithography techniques by exploiting either electron-beam, focused ion-beam, nanoimprint, or interference lithography on a rigid, flat wafer.[18−21] Despite great successes over the past decades, these approaches are limited by the laborious, complex, and time-consuming nature of the nanolithography techniques, thereby impeding their application in wide-ranging use. Recently, we demonstrated a proof-of-concept methodology that enables the physical transfer of quasi-3D metal−dielectric hybrid nanoarchitectures from their donor Si molds to a foreign receiver substrate (e.g., photodetectors) in a time- and cost-effective manner.[22] However, this method, as well as any other similar method, has never been applicable to infrared (IR) filters due to the inherent extreme brittleness of IR-transparent dielectric spacers, such as SU-8 (i.e., fracture strain = 2−3%).[23]

Here, we unlocked this material limitation to establish mechanically and optically reliable IR filters built upon quasi-3D metal−dielectric hybrid nanoantennas using an SU-8 dielectric spacer. The entire fabrication process of the IR filters occurred at room temperature with a temporary stress-absorbing layer, such as poly(methyl methacrylate) (PMMA), to prevent the extremely brittle SU-8 dielectric spacer from having mechanical damage. Following a complete removal of the stress-absorbing layer, the resulting IR filters offered a capability of spectral filtering in the IR region with respect to the peak transmission and full width at half-maximum (fwhm). We investigated the effect of their structural designs on IR bandpass filtering and also validated

Received: March 1, 2021
Accepted: May 5, 2021
Published: May 14, 2021

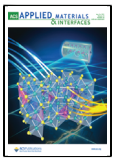

https://doi.org/10.1021/acsami.1c03932
ACS Appl. Mater. Interfaces 2021, 13, 24024−24031

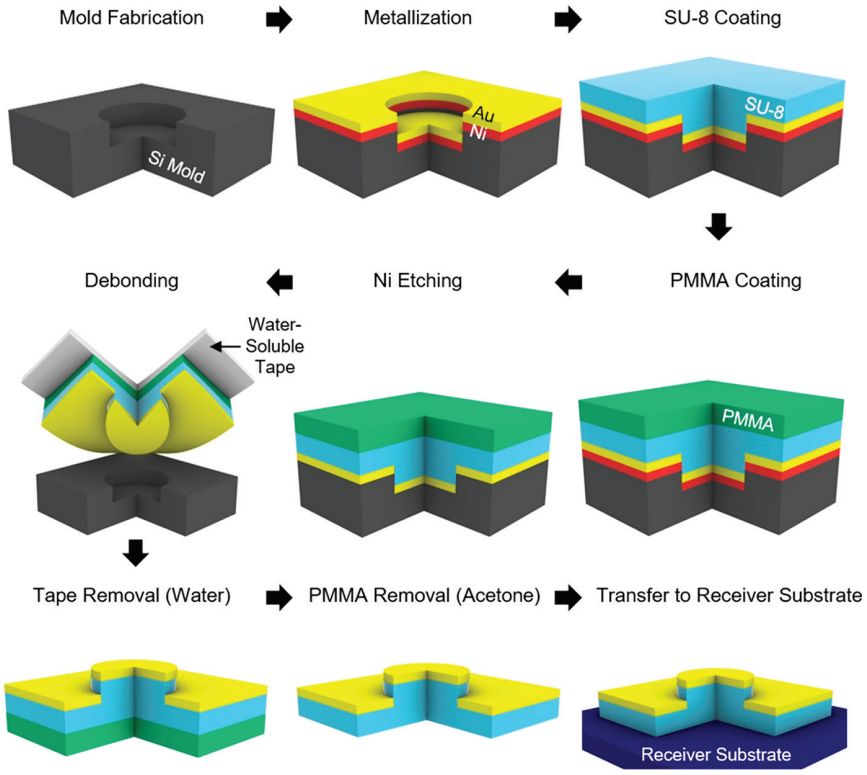

Figure 1. Schematic illustrations for the fabrication process of a single unit of a quasi-3D metal (i.e., Au)−dielectric (i.e., SU-8) nanopost.

the experimental results with computational analysis using the finite integration technique (FIT) and finite element method (FEM).

RESULTS AND DISCUSSION

Repetitive Replication of Quasi-3D Plasmonic IR Filters. Figure 1 schematically illustrates the fabrication process of the IR filters, which begins with a Si mold that contains preformed quasi-3D nanoposts or nanoholes via a lithographic patterning. The fabrication process of the Si mold is also schematically illustrated in Figure S1 with the detailed experimental procedures in the Materials and Methods section. First, thin films of Ni (10 nm)/Au (50 nm) were deposited on the Si mold using an e-beam evaporator, followed by the deposition of SU-8 (600 nm)/PMMA (1 μm) via spin-casting. Next, the entire structure was immersed in a bath of Ni etchant (TFB, Transene) to selectively etch the underneath Ni layer, and then rinsed with distilled water. A water-soluble tape (Aquasol) was attached on the top surface of the PMMA layer, and then gently peeled off, allowing the remaining thin films (i.e., Au/SU-8/PMMA) to be cleanly delaminated from the Si mold. Both the water-soluble tape and the PMMA layer were then removed by placing on a bath of water and acetone sequentially. The underlying mechanics of this defect-free debonding process are discussed in the following section. Finally, the resulting structure (i.e., Au/SU-8) was transferred to a desired receiver substrate.

Here, the SU-8 layer was used not only to serve as an IR-transparent dielectric spacer through which the light can transmit at a wavelength of 3−10 μm but also to be thinly spin-coated in the submicrometer range (i.e., <600 nm thick).[25,26] The minimum achievable thickness of the SU-8 layer was approximately 150 nm which is at least 26-fold thinner than that of other dielectric materials such as Ecoflex (i.e., >4 μm thick) using a diluent thinning agent such as SU-8 2000 Thinner (MicroChem, Inc.) and Thinning Ecoflex Silicones (Smooth-on, Inc.), respectively (Figure S2a). Therefore, the IR filters using an SU-8 dielectric spacer enabled advances in providing a stable transmission spectrum over the counterpart using an Ecoflex dielectric spacer (Figure S2b) despite their similar optical transparency in an IR regime (Figure S2c).

Figure 2a shows schematic diagrams of a single unit of a metal (i.e., Au)−dielectric (i.e., SU-8) IR filter configured into quasi-3D nanoposts (left panel) and nanoholes (right panel), respectively. The geometrical parameters of the IR filters are denoted as follows: periodicity (p), diameter of the Au disks (d), height or depth of the quasi-3D nanoposts and nanoholes (t_p), thickness of the perforated Au film (t_m), and thickness of the dielectric spacer (t_d). Figure 2b presents a series of optical and scanning electron microscopy (SEM) images of the transferred quasi-3D nanoposts (left panel) and nanoholes (right panel) on a double-side polished (DSP) Si wafer (UniversityWafer), respectively. The results exhibited no evidence of visible damage or defects across the entire surface of the IR filters. The enlarged tilted-angle and cross-sectional views of the SEM images (bottom panels) highlight the clear physical separation at the gap between the SU-8 spacer and the Au arrays without degradation. Importantly, the donor Si mold was intact throughout the entire process, allowing it to be reused for multiple replication of the IR filters with a piranha cleaning after each use (Figure S3). The replicability of the Si mold can obviate the need for iterative implementation of e-beam lithography that has been typically required for current approaches.

Underlying Mechanism of the Defect-Free Replication Process. The defect-free replication of the IR filters, even

https://doi.org/10.1021/acsami.1c03932
ACS Appl. Mater. Interfaces 2021, 13, 24024−24031

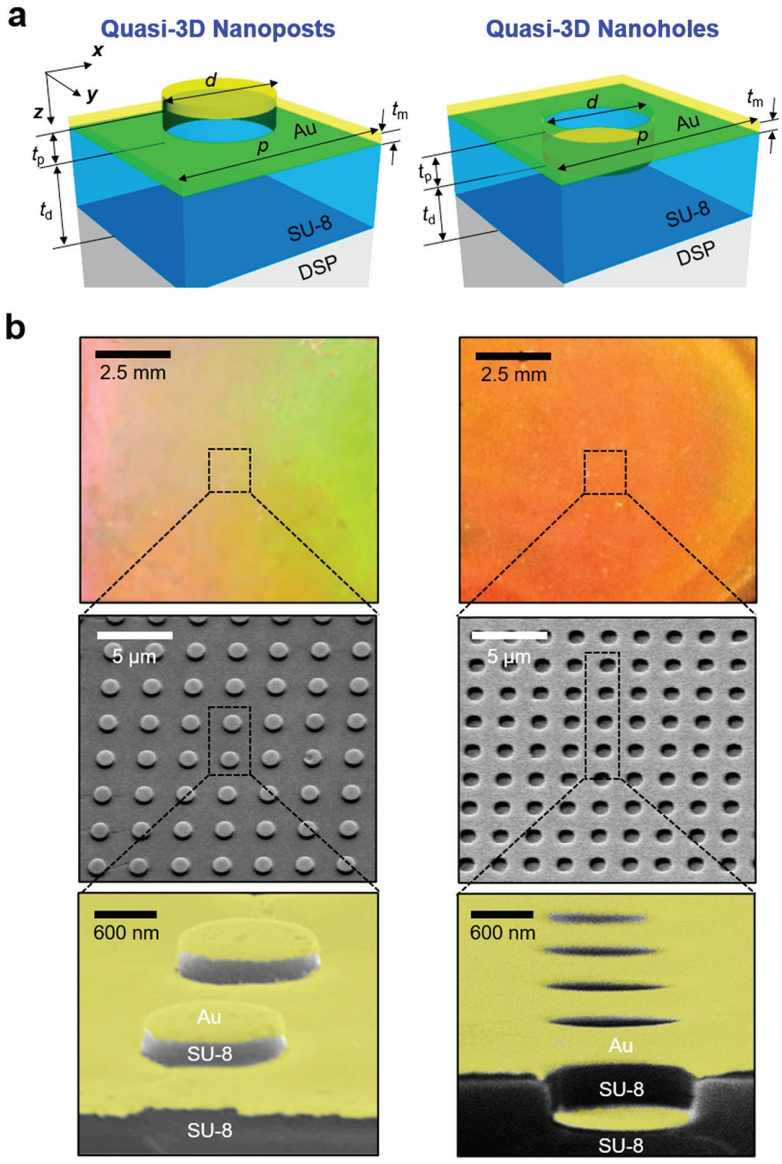

Figure 2. (a) Schematic diagrams of a single unit of quasi-3D nanoposts (left panel) and nanoholes (right panel). (b) The corresponding optical and SEM images of the transferred quasi-3D nanoposts (left panel) and nanoholes (right panel) on a receiver substrate.

with the extremely brittle SU-8 spacer, is attributed to the use of the temporary stress-absorbing layer (i.e., PMMA) that is capable of efficiently accommodating induced strains under mechanical deformations (i.e., debonding process). Figure 3a (left panel) presents the FEM results displaying the distribution of principal strain (ε) for a 3 × 3 array of quasi-3D nanoposts (p = 3 μm; d = 1.2 μm; t_m = 50 nm; t_p = 250 nm; t_d = 400 nm) with (top panel) and without (bottom panel) a PMMA layer (1 μm) under the debonding process at the minimum required peeling force of 40 mN. The inset images present that the maximum strains (ε_{max}) of 7% and 4% appeared at the edge of the quasi-3D nanoposts and nanoholes where the stresses are concentrated, respectively. The corresponding FEM results for the entire debonding process are shown in Movie S1. For comparison, Figure S4 shows the corresponding FEM results in the presence of the interfacial adhesion (200 MPa) using a single unit of quasi-3D nanopost (left panel) and nanohole (right panel) with the Si mold. The ε_{max} of the quasi-3D nanoposts was <1.8% with the presence of the PMMA layer, which is below the fracture limit of the SU-8 spacer (ε = 2−3%),[23] whereas the ε_{max} of the quasi-3D nanoposts increased up to 7.1% with the absence of the PMMA layer, which thereby may lead to cracking through the SU-8 dielectric spacer. The corresponding results for a 3 × 3 array of quasi-3D nanoholes (p = 3 μm; d = 1.2 μm; t_m = 50 nm; t_p = 330 nm; t_d = 230 nm) are shown in Figure 3a (right panel), producing consistent outcomes. The ε_{max} of the quasi-3D nanoholes decreased from 3.7% to 1.2%, by more than 3-fold, with the presence of the PMMA layer. These results confirm that the PMMA layer is effective at protecting the brittle SU-8 spacer from fracture throughout the debonding process. This is mainly attributed to the increased bending stiffness of the entire structure with the presence of the PMMA layer. Figure 3b presents the bending stiffness (blue dotted line) and the ε_{max} (black dotted line) of the quasi-3D nanoposts (left panel) and nanoholes (right panel) as a function of the PMMA thickness, respectively. The bending stiffness dramatically increased from 0.3 to 28 × 10^3 GPa·μm^4

https://doi.org/10.1021/acsami.1c03932
ACS Appl. Mater. Interfaces 2021, 13, 24024−24031

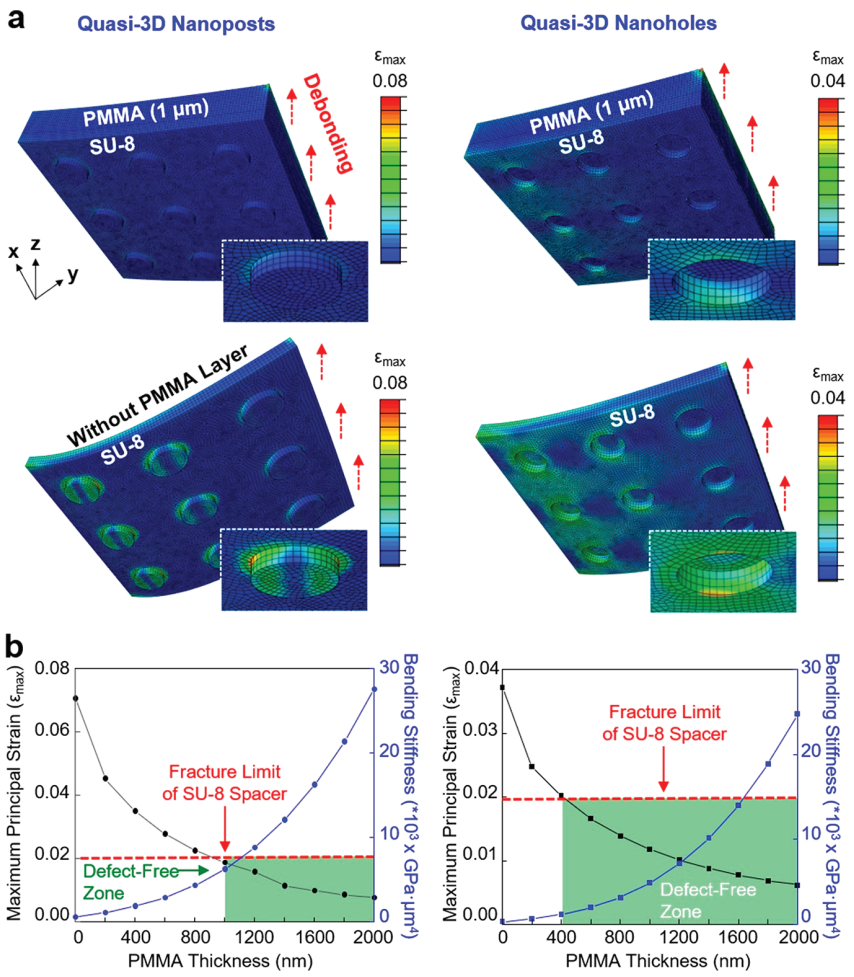

Figure 3. (a) FEM results displaying the distribution of ε for the quasi-3D nanoposts (left panel) and nanoholes (right panel) with (top panel) and without (bottom panel) the presence of a PMMA layer during debonding. (b) The corresponding bending stiffness (blue dotted line) and ε_{max} (black dotted line) of the quasi-3D nanoposts (left panel) and nanoholes (right panel) as a function of the PMMA thickness.

with the increased PMMA thickness from 0 to 2 μm, which also resulted in an exponential decrease of the ε_{max} for both the quasi-3D nanoposts and nanoholes. The green-filled area in these graphs indicates a zone where a defect-free debonding process occurred at ε_{max} below the fracture limit of the SU-8 spacer (ε = 2−3%).[23] The results also indicate that the PMMA layer is required to be thicker than at least 1 and 0.4 μm for the defect-free debonding of the quasi-3D nanoposts and nanoholes, respectively. Representative images of a damaged IR filter that includes a PMMA layer thinner than these thresholds are shown in Figure S5.

Figure S6a shows the schematic illustration of a 3 × 3 square array of the quasi-3D nanoposts (left panel) and nanoholes (right panel) under debonding from an edge, respectively. The dashed lines denote the surface topology along the i−i' and j−j' directions. The corresponding FEM results in Figure S6b reveal the local strains of the quasi-3D nanoposts (left panel) and nanoholes (right panel) with (black dotted lines) and without (red dotted lines) the presence of a PMMA layer (1 μm). Without the PMMA layer, the peak strains were sharply localized at the edges of the quasi-3D nanoposts and nanoholes along both directions. The localized peak strains were attenuated along the direction of applied peeling force (i.e., the i−i' direction), while they were unchanged in its perpendicular direction (i.e., the j−j' direction). Overall, the localized peak strains along the i−i' direction were larger than those along the j−j' direction, all of which were beyond or near the fracture limit of the SU-8 spacer (ε = 2−3%).[23] These results imply that cracks were initiated most likely at the edge of where the peeling force was applied, and then propagated along the i−i' direction more than the j−j' direction, as also evidenced in Figure S5. With the PMMA layer, the sharp localization of peak strains at the edges of the quasi-3D nanoposts and nanoholes was alleviated due to the stress-absorbing effect. This also resulted in a substantial reduction of the localized peak strains, by at least 57%, below the fracture limit of the SU-8 spacer along the both directions. These observations were consistent with experimental observations, providing an important insight into identifying optimal conditions for the defect-free debonding of various quasi-3D nanoarchitectures with high-fidelity.

Application in IR Bandpass Filtering. Figure 4a shows experimental (red dotted line) and computational (blue dotted line) results for the transmission filter effect of the quasi-3D nanoposts (left panel) and nanoholes (right panel), respectively. The transmissions of these IR filters were measured at normal incidence using a Fourier transform infrared (FTIR) spectrometer (Nicolet 5700) in a wavelength range of 2.5−

https://doi.org/10.1021/acsami.1c03932
ACS Appl. Mater. Interfaces 2021, 13, 24024−24031

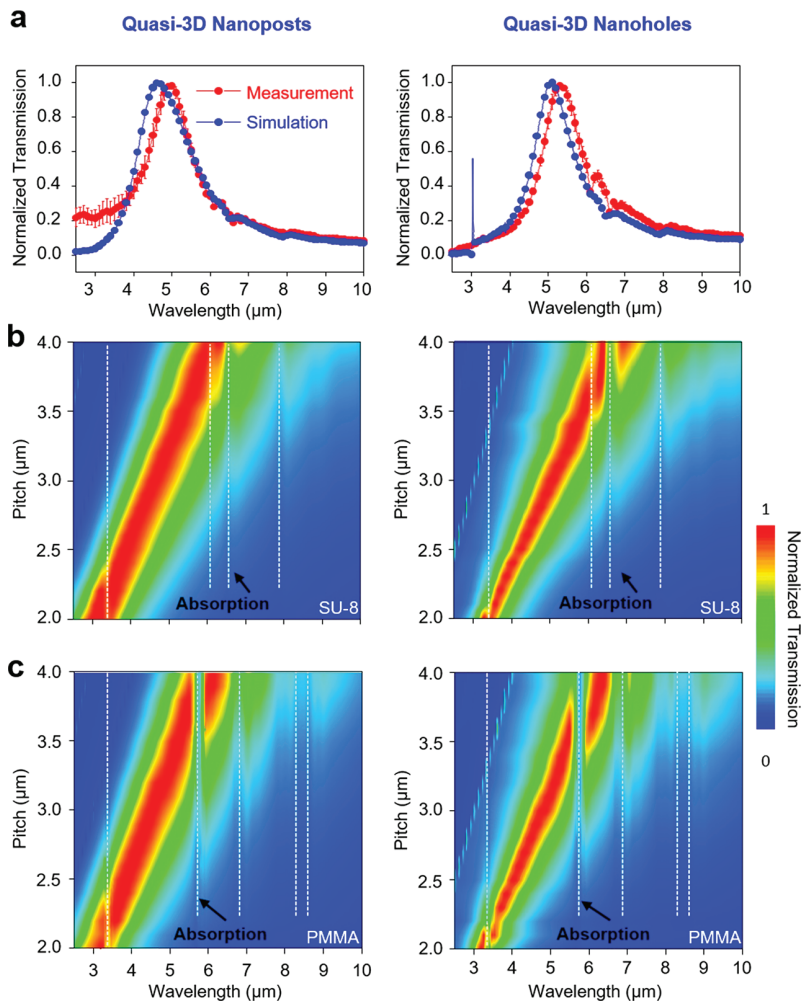

Figure 4. (a) Experimental (red dotted line) and computational (blue dotted line) results for the transmission filter effect of the quasi-3D nanoposts (left panel) and nanoholes (right panel). (b) 2D surface plots for the normalized transmission of the quasi-3D nanoposts (left panel) and nanoholes (right panel) as functions of wavelength and periodicity (p). (c) Corresponding results of the IR filters that contain a PMMA spacer as a control comparison.

10.0 μm. An unpolarized FTIR beam was used to measure the transmission. The numerical simulations were performed using a 3D FIT solver (CST Microwave Studio), as detailed in the Materials and Methods section. The results show that bandpass filtering occurred within an IR range at the peak wavelengths of 4.9 and 5.3 μm for the quasi-3D nanoposts and nanoholes, respectively. The corresponding fwhm's occurred at the peak wavelengths of 1.4 and 1.3 μm, respectively. The experimental and computational results were in agreement with a discrepancy of less than 7% (peak wavelength) and 2% (fwhm), which may come from imperfection and variation in the fabrication of the Si molds. In addition, the repetitive transmission spectra measured across the area (1×1 cm^2) of the transferred quasi-3D nanoposts and nanoholes showed very good uniformity with only small variations in spectra.

Figure 4b shows the 2D surface plots of normalized transmission for the quasi-3D nanoposts (left panel) and nanoholes (right panel) as functions of wavelength and periodicity (p), respectively. The results exhibited a clear spectral shift of the transmission peak toward a longer wavelength for both the nanoposts (from 3.2 to 6.0 μm) and nanoholes (from 3.3 to 6.3 μm) as the p increased from 2 to 4 μm. For instance, relatively weak absorptions occurred at wavelengths of 3.3, 6.2, 6.6, and 8 μm. The peak wavelength and fwhm of these IR filters were tunable through the adjustment of their geometrical parameters such as d, t_p, t_m, and t_d within the ranges of 3−6 μm and 0.5−2.5 μm, respectively (Figure S7). Here, the t_d is a critical parameter to determine a Fabry−Perot optical cavity through which multiple light reflections occur between the perforated Au film and the Si top surface.[27] The peak wavelength is susceptible to any change of the gap space ($t_g = t_p - t_m$) between the perforated Au film and the Au disks which results in the spectral shift of a localized surface plasmon resonance wavelength.[28] Specifically, a red-shifting of the peak wavelength occurs as the t_p decreases or the t_m increases due to an excited electric field at the edge of the Au disks via a localized surface plasmon resonance.[29] Therefore, any residual deposition of Au to the sidewall of the quasi-3D nanoposts and nanoholes apparently affects the performance of the IR filters due to the reduced gap space (t_g) (Figure S8). Figure 4c shows the corresponding results of the quasi-3D nanoposts (left panel) and nanoholes (right panel) that contain a PMMA spacer (1 μm thick) as a control comparison, respectively. The results

https://doi.org/10.1021/acsami.1c03932
ACS Appl. Mater. Interfaces 2021, 13, 24024−24031

show that strong spectral interferences (i.e., the absorption of IR radiation) occurred at wavelengths of 3.3, 5.8, 7.0, 8.3, and 8.7 μm due to the stretching vibration of C−O−C and C−H bonds in the PMMA spacer, thereby hindering IR bandpass filtering.[29]

CONCLUSION

The key findings of this study revealed the underlying mechanisms of a new method enabling the repetitive replication of quasi-3D plasmonic IR filters from their Si molds, even with the presence of an extremely brittle IR-transparent spacer such as SU-8. The fundamental understanding of the underlying fracture mechanics enabled the multiple reuse of the donor Si molds without degradation, thereby overcoming the key challenges of current approaches that typically involve the iterative implementation of nanolithography techniques. The high replicability of the Si molds could lead to a significant reduction of cost and time for the production of various IR filters of interests. The quality, reliability, and performance of the resulting IR filters were validated through experimental and computational analyses, suggesting a route for their pragmatic application in multispectral imaging systems.

MATERIALS AND METHODS

Fabrication of the Donor Si Mold. The fabrication of a donor Si mold began by producing an array of circle-shaped apertures (i.e., nanoposts or nanoholes) on a Si wafer via a photolithographic patterning using a photoresist (MicroChemicals). A thin layer (20 nm thick) of Cr was then deposited to serve as a mask layer using an e-beam evaporator. A predominately anisotropic CF_4/O_2 plasma reactive ion etch (RIE) was applied to generate an undercut at the RF power of 100 W with CF_4 (13 sccm) and O_2 (2 sccm) gases under the pressure of 45 mTorr. Finally, the Cr mask layer was removed by immersion in a bath of a Cr etchant (Transene 1020) for 30 s to complete a Si mold. The orthogonal pitches of both the 2D gratings p_x (pitch along x-axis) and the p_x (pitch along y-axis) were fixed at 3.0 μm ($p_x = p_x = p$). The diameter of the circular nanoposts or nanoholes was fixed at 1.2 μm.

Numerical Simulation of Transmission. Numerical simulation was performed using a commercial 3D FIT solver (CST Microwave Studio).[30] This simulation was to obtain the transmission spectra of the nanoantennas and therefore to understand the underlying physics and optics including the Fabry−Perot optical cavity, guided-mode resonance, localized surface plasmon resonance, and surface plasmonic resonance.[31−37] As schematically illustrated in Figure 1, parts a and b, we implemented a single unit cell with appropriate boundary conditions that include (1) a perfect magnetic conductor (PMC for short, $H_t = 0$) in the x−z plane, (2) a perfect electric conductor (PEC for short, $E_t = 0$) in the y−z plane, and (3) a transverse electromagnetic (TEM) plane wave propagating in the z-direction. The direction of polarized incoming light was set to be parallel to the x-axis. We obtained the wavelength-dependent complex S-parameters, S_{ij}, where the subscripts i and j represent the waveguide ports at the Si substrate and air, respectively. The simulated transmission from j (air) to i (Si) was calculated by $|S_{ij}|^2$. The refractive index of Si was taken as $n_{Si} = 3.42$.[38] The Au was defined by the Drude model with the plasma frequency of $w_p = 1.38 \times 10^{16}$ Hz and the collision frequency of $w_c = 5.71 \times 1013$ Hz.[39] The values of the real and imaginary parts of the permittivity in SU-8 and PMMA were used from the literatures.[24,29]

FEM Analysis. The FEM analysis was performed using a commercial ABAQUS/standard package (Dassault Systems).[40] The materials used in this study (e.g., Au, SU-8, and PMMA) were modeled by C3D8R elements (8 nodes linear brick; reduced integration solid elements). These materials were deformed by elastic behavior with the mechanical modulus (E) of 77.2, 4.1, and 3 GPa and the Poisson's ratio (ν) of 0.42, 0.22, and 0.37, respectively.[41−43] The pulling force (40 mN) to initiate the delamination was applied at a corner of the IR filters, as shown in Figure 3.

FTIR measurements. The normal-incidence transmission was measured using an FTIR spectrometer (Nicolet 5700) in a wavelength range of 2.5−10.0 μm using a KBr beam splitter and a mercury−cadmium telluride (MCT) detector. The transmission spectra were recorded with a resolution of 4 cm^{-1}. A square pinhole (1 mm × 1 mm) was used to measure the structural uniformity of the IR filters across a large area (1 × 1 cm^2).

ASSOCIATED CONTENT

Supporting Information

The Supporting Information is available free of charge at https://pubs.acs.org/doi/10.1021/acsami.1c03932.

Schematic illustrations for the fabrication process of a donor Si mold, thickness of the dielectric spacer using SU-8 and Ecoflex diluted with SU-8 2000 Thinner and Thinning Ecoflex Silicones, respectively, simulated transmission spectra as a function of wavelength for the IR filters using SU-8, SU-8, and Ecoflex as a dielectric spacer, transmission spectrum of SU-8 and Ecoflex at varied thicknesses, SEM images of a representative Si mold throughout multiple replication processes, FEM results displaying the distribution of ε for the quasi-3D nanoposts and nanoholes without and with interfacial adhesion with the Si mold, representative SEM image of the damaged IR filters when processed out of the defect-free zone, schematic illustration for the quasi-3D nanoposts and nanoholes during debonding from an edge, local strains of the quasi-3D nanoposts and nanoholes with and without the presence of a PMMA layer, representative results of peak wavelength and fwhm for the quasi-3D nanoposts and nanoholes with varied geometric parameters, schematic illustrations of a single unit of the quasi-3D nanoposts and nanoholes, and simulated peak wavelength with the reduced gap space by the sidewall deposition of Au (PDF)

FEM results for the entire debonding process (MP4)

AUTHOR INFORMATION

Corresponding Authors

Chi Hwan Lee − *School of Mechanical Engineering, Weldon School of Biomedical Engineering, and Department of Materials Engineering, Purdue University, West Lafayette, Indiana 47907, United States*; orcid.org/0000-0002-4868-7054; Email: lee2270@purdue.edu

Zahyun Ku − *Materials and Manufacturing Directorate, Air Force Research Laboratory, Wright-Patterson Air Force Base 45433, United States*; Email: zahyun.ku.1.ctr@us.af.mil

Authors

Bongjoong Kim − *School of Mechanical Engineering, Purdue University, West Lafayette, Indiana 47907, United States*; orcid.org/0000-0002-9969-6954

Jehwan Hwang − *Weldon School of Biomedical Engineering, Purdue University, West Lafayette, Indiana 47907, United States*

Jonghun Yi − *School of Mechanical Engineering, Hanyang University, Seoul 04763, Republic of Korea*

https://doi.org/10.1021/acsami.1c03932
ACS Appl. Mater. Interfaces 2021, 13, 24024−24031

Dong Rip Kim − *School of Mechanical Engineering, Hanyang University, Seoul 04763, Republic of Korea;* orcid.org/0000-0001-6398-9483

Augustine Urbas − *Materials and Manufacturing Directorate, Air Force Research Laboratory, Wright-Patterson Air Force Base 45433, United States*

Complete contact information is available at: https://pubs.acs.org/10.1021/acsami.1c03932

Author Contributions

#B.K. and J.H. contributed equally to this work.

Notes

The authors declare no competing financial interest.

■ ACKNOWLEDGMENTS

This project was supported by the National Science Foundation (NSF: CMMI-1928784 and CMMI-1728149). Z.K. also acknowledges support from the Asian Office of Aerospace Research and Development (AOARD: FA2386-18-1-4104). D.R.K. acknowledges the International Research and Development Program (NRF-2018K1A3A1A32055469) through the National Research Foundation of Korea (NRF) funded by the Ministry of Science and ICT of Korea. J.Y. acknowledges the funding support from the MOTIE (Ministry of Trade, Industry, and Energy) in Korea, under the Fostering Global Talents for Innovative Growth Program (P0008748, Global Human Resource Development for Innovative Design in Robot and Engineering) supervised by the Korea Institute for Advancement of Technology (KIAT).

■ REFERENCES

(1) Amenabar, I.; Poly, S.; Goikoetxea, M.; Nuansing, W.; Lasch, P.; Hillenbrand, R. Hyperspectral Infrared Nanoimaging of Organic Samples Based on Fourier Transform Infrared Nanospectroscopy. *Nat. Commun.* **2017**, *8*, 14402.

(2) Yakovliev, A.; Ziniuk, R.; Wang, D.; Xue, B.; Vretik, L. O.; Nikolaeva, O. A.; Tan, M.; Chen, G.; Slominskii, Y. L.; Qu, J.; et al. Hyperspectral Multiplexed Biological Imaging of Nanoprobes Emitting in the Short-Wave Infrared Region. *Nanoscale Res. Lett.* **2019**, *14*, 243.

(3) Duempelmann, L.; Gallinet, B.; Novotny, L. Multispectral Imaging with Tunable Plasmonic Filters. *ACS Photonics* **2017**, *4*, 236−241.

(4) Meng, J.; Cadusch, J. J.; Crozier, K. B. Plasmonic Mid-Infrared Filter Array-Detector Array Chemical Classifier Based on Machine Learning. *ACS Photonics* **2021**, *8*, 648−657.

(5) Primpke, S.; Godejohann, M.; Gerdts, G. Rapid Identification and Quantification of Microplastics in the Environment by Quantum Cascade Laser-Based Hyperspectral Infrared Chemical Imaging. *Environ. Sci. Technol.* **2020**, *54*, 15893−15903.

(6) Ghaderi, M.; Ayerden, N. P.; Emadi, A.; Enoksson, P.; Correia, J. H.; de Graaf, G.; Wolffenbuttel, R. F. Design, Fabrication and Characterization of Infrared LVOFs for Measuring Gas Composition. *J. Micromech. Microeng.* **2014**, *24*, 084001.

(7) Zhang, S.; Bin, W.; Xu, B.; Zheng, X.; Chen, B.; Lv, X.; San, H.; Hofmann, W. Mixed-Gas $CH_4/CO_2/CO$ Detection Based on Linear Variable Optical Filter and Thermopile Detector Array. *Nanoscale Res. Lett.* **2019**, *14*, 348.

(8) Emadi, A.; Wu, H.; de Graaf, G.; Wolffenbuttel, R. Design and Implementation of a Sub-nm Resolution Microspectrometer Based on a Linear-Variable Optical Filter. *Opt. Express* **2012**, *20*, 489−507.

(9) Craig, B.; Shrestha, V. R.; Meng, J.; Cadusch, J. J.; Crozier, K. B. Experimental Demonstration of Infrared Spectral Reconstruction Using Plasmonic Metasurfaces. *Opt. Lett.* **2018**, *43*, 4481−4484.

(10) Tan, X.; Zhang, H.; Li, J.; Wan, H.; Guo, Q.; Zhu, H.; Liu, H.; Yi, F. Non-Dispersive Infrared Multi-Gas Sensing Via Nanoantenna Integrated Narrowband Detectors. *Nat. Commun.* **2020**, *11*, 5245.

(11) Jeon, J.; Bhattarai, K.; Kim, D.-K.; Kim, J. O.; Urbas, A.; Lee, S. J.; Ku, Z.; Zhou, J. A Low-Loss Metasurface Antireflection Coating on Dispersive Surface Plasmon Structure. *Sci. Rep.* **2016**, *6*, 36190.

(12) Yoo, D.; Vidal-Codina, F.; Ciracì, C.; Nguyen, N.-C.; Smith, D. R.; Peraire, J.; Oh, S.-H. Modeling and Observation of Mid-Infrared Nonlocality in Effective Epsilon-near-Zero Ultranarrow Coaxial Apertures. *Nat. Commun.* **2019**, *10*, 4476.

(13) Shah, Y. D.; Grant, J.; Hao, D.; Kenney, M.; Pusino, V.; Cumming, D. R. S. Ultra-Narrow Line Width Polarization-Insensitive Filter Using a Symmetry-Breaking Selective Plasmonic Metasurface. *ACS Photonics* **2018**, *5*, 663−669.

(14) Azad, A. K.; O'Hara, J. F.; Singh, R.; Chen, H.; Taylor, A. J. A Review of Terahertz Plasmonics in Subwavelength Holes on Conducting Films. *IEEE J. Sel. Top. Quantum Electron.* **2013**, *19*, 8400416−8400416.

(15) Lin, Y.-S.; Liao, S.; Liu, X.; Tong, Y.; Xu, Z.; Xu, R.; Yao, D.; Yu, Y. Tunable Terahertz Metamaterial by Using Three-Dimensional Double Split-Ring Resonators. *Opt. Laser Technol.* **2019**, *112*, 215−221.

(16) Vial, B.; Commandré, M.; Demésy, G.; Nicolet, A.; Zolla, F.; Bedu, F.; Dallaporta, H.; Tisserand, S.; Roux, L. Transmission Enhancement through Square Coaxial Aperture Arrays in Metallic Film: When Leaky Modes Filter Infrared Light for Multispectral Imaging. *Opt. Lett.* **2014**, *39*, 4723−4726.

(17) Fernández-Domínguez, A. I.; García-Vidal, F. J.; Martín-Moreno, L. Unrelenting Plasmons. *Nat. Photonics* **2017**, *11*, 8−10.

(18) Staude, I.; Schilling, J. Metamaterial-Inspired Silicon Nanophotonics. *Nat. Photonics* **2017**, *11*, 274−284.

(19) Joshi-Imre, A.; Bauerdick, S. Direct-Write Ion Beam Lithography. *J. Nanotechnol.* **2014**, *2014*, 170415.

(20) Gao, L.; Shigeta, K.; Vazquez-Guardado, A.; Progler, C. J.; Bogart, G. R.; Rogers, J. A.; Chanda, D. Nanoimprinting Techniques for Large-Area Three-Dimensional Negative Index Metamaterials with Operation in the Visible and Telecom Bands. *ACS Nano* **2014**, *8*, 5535−5542.

(21) Huo, P.; Zhang, S.; Liang, Y.; Lu, Y.; Xu, T. Hyperbolic Metamaterials and Metasurfaces: Fundamentals and Applications. *Adv. Opt. Mater.* **2019**, *7*, 1801616.

(22) Kim, B.; Jeon, J.; Zhang, Y.; Wie, D. S.; Hwang, J.; Lee, S. J.; Walker, D. E.; Abeysinghe, D. C.; Urbas, A.; Xu, B.; Ku, Z.; Lee, C. H. Deterministic Nanoassembly of Quasi-Three-Dimensional Plasmonic Nanoarrays with Arbitrary Substrate Materials and Structures. *Nano Lett.* **2019**, *19*, 5796−5805.

(23) Robin, C. J.; Vishnoi, A.; Jonnalagadda, K. N. Mechanical Behavior and Anisotropy of Spin-Coated SU-8 Thin Films for Mems. *J. Microelectromech. Syst.* **2014**, *23*, 168−180.

(24) Digaum, J. L.; Pazos, J. J.; Chiles, J.; D'Archangel, J.; Padilla, G.; Tatulian, A.; Rumpf, R. C.; Fathpour, S.; Boreman, G. D.; Kuebler, S. M. Tight Control of Light Beams in Photonic Crystals with Spatially-Variant Lattice Orientation. *Opt. Express* **2014**, *22*, 25788−25804.

(25) Ashraf, S.; Niskanen, I.; Kanyathare, B.; Vartiainen, E.; Mattsson, C.; Heikkilä, R.; Thungström, G. Determination of Complex Refractive Index of SU-8 by Kramers−Kronig Dispersion Relation Method at the Wavelength Range 2.5−22.0 μm. *J. Quant. Spectrosc. Radiat. Transfer* **2019**, *224*, 309−311.

(26) Chanda, D.; Shigeta, K.; Truong, T.; Lui, E.; Mihi, A.; Schulmerich, M.; Braun, P. V.; Bhargava, R.; Rogers, J. A. Coupling of Plasmonic and Optical Cavity Modes in Quasi-Three-Dimensional Plasmonic Crystals. *Nat. Commun.* **2011**, *2*, 479.

(27) Wang, C.; Zhang, Q.; Song, Y.; Chou, S. Y. Plasmonic Bar-Coupled Dots-on-Pillar Cavity Antenna with Dual Resonances for Infrared Absorption and Sensing: Performance and Nanoimprint Fabrication. *ACS Nano* **2014**, *8*, 2618−2624.

(28) Li, W.-D.; Ding, F.; Hu, J.; Chou, S. Y. Three-Dimensional Cavity Nanoantenna Coupled Plasmonic Nanodots for Ultrahigh and

Uniform Surface-Enhanced Raman Scattering over Large Area. *Opt. Express* **2011**, *19*, 3925−3936.
(29) Jitian, S.; Bratu, I. Determination of Optical Constants of Polymethyl Methacrylate Films from IR Reflection-Absorption Spectra. *AIP Conf. Proc.* **2012**, *1425*, 26.
(30) *CST Studio Suite*; Dassault Systemes Simulia Corporation: Providence, RI. 2020.
(31) Montoya, J. A.; Tian, Z.-B.; Krishna, S.; Padilla, W. J. Ultra-Thin Infrared Metamaterial Detector for Multicolor Imaging Applications. *Opt. Express* **2017**, *25*, 23343−23355.
(32) Lee, S. J.; Ku, Z.; Barve, A.; Montoya, J.; Jang, W.-Y.; Brueck, S. R. J.; Sundaram, M.; Reisinger, A.; Krishna, S.; Noh, S. K. A Monolithically Integrated Plasmonic Infrared Quantum Dot Camera. *Nat. Commun.* **2011**, *2*, 286.
(33) Ooi, K. J. A.; Chu, H. S.; Ang, L. K.; Bai, P. Mid-Infrared Active Graphene Nanoribbon Plasmonic Waveguide Devices. *J. Opt. Soc. Am. B* **2013**, *30*, 3111−3116.
(34) Huang, E. K.-w.; Hoang, M.-A.; Chen, G.; Ramezani-Darvish, S.; Haddadi, A.; Razeghi, M. Highly Selective Two-Color Mid-Wave and Long-Wave Infrared Detector Hybrid Based on Type-II Superlattices. *Opt. Lett.* **2012**, *37*, 4744−4746.
(35) Huang, E. K.-w.; Haddadi, A.; Chen, G.; Nguyen, B.-M.; Hoang, M.-A.; McClintock, R.; Stegall, M.; Razeghi, M. Type-II Superlattice Dual-Band LWIR Imager with M-Barrier and Fabry−Perot Resonance. *Opt. Lett.* **2011**, *36*, 2560−2562.
(36) Liang, C.; Yi, Z.; Chen, X.; Tang, Y.; Yi, Y.; Zhou, Z.; Wu, X.; Huang, Z.; Yi, Y.; Zhang, G. Dual-Band Infrared Perfect Absorber Based on a Ag-Dielectric-Ag Multilayer Films with Nanoring Grooves Arrays. *Plasmonics* **2020**, *15*, 93−100.
(37) Hess, O.; Pendry, J. B.; Maier, S. A.; Oulton, R. F.; Hamm, J. M.; Tsakmakidis, K. L. Active Nanoplasmonic Metamaterials. *Nat. Mater.* **2012**, *11*, 573−584.
(38) Cetin, R.; Akin, T. Numerical and Experimental Investigation into LWIR Transmission Performance of Complementary Silicon Subwavelength Antireflection Grating (Swarg) Structures. *Sci. Rep.* **2019**, *9*, 4683.
(39) Fowler, C.; Kim, J. O.; Lee, S. J.; Urbas, A.; Ku, Z.; Zhou, J. Strong Responsivity Enhancement of Quantum Dot-in-a-Well Infrared Photodetectors Using Plasmonic Structures. *Adv. Theory Simul.* **2019**, *2*, 1800143.
(40) *Abaqus Standard*; Dassault Systemes Simulia Corporation: Providence, RI. 2016.
(41) Fang, Z.; Geng, Y.; Wang, J.; Yan, Y.; Zhang, G. Mechanical Properties of Gold Nanowires Prepared by Nanoskiving Approach. *Nanoscale* **2020**, *12*, 8194−8199.
(42) Xu, T.; Yoo, J. H.; Babu, S.; Roy, S.; Lee, J.-B.; Lu, H. Characterization of the Mechanical Behavior of SU-8 at Microscale by Viscoelastic Analysis. *J. Micromech. Microeng.* **2016**, *26*, 105001.
(43) Samuel, C.; Raquez, J.-M.; Dubois, P. PLLA/PMMA Blends: A Shear-Induced Miscibility with Tunable Morphologies and Properties? *Polymer* **2013**, *54*, 3931−3939.

https://doi.org/10.1021/acsami.1c03932
ACS Appl. Mater. Interfaces 2021, 13, 24024−24031